Tail state formation in solar cell materials: First principles analyses of zincblende, chalcopyrite, kesterite, and hybrid perovskite crystals

Mitsutoshi Nishiwaki,[1] Keisuke Nagaya,[1] Masato Kato,[1] Shohei Fujimoto,[1] Hitoshi Tampo,[2] Tetsuhiko Miyadera,[2] Masayuki Chikamatsu,[2] Hajime Shibata,[2] and Hiroyuki Fujiwara[1,*]

[1]*Department of Electrical, Electronic and Computer Engineering, Gifu University, 1-1 Yanagido, Gifu 501-1193, Japan*

[2]*Research Center for Photovoltaics, National Institute of Advanced Industrial Science and Technology (AIST), Central2, 1-1-1 Umezono, Tsukuba, Ibaraki 305-8568, Japan*

(Received 30 January 2018; revised manuscript received 19 June 2018; published 10 August 2018)

Tail state formation in solar cell absorbers leads to a detrimental effect on solar cell performance. Nevertheless, the characterization of the band tailing in experimental semiconductor crystals is generally difficult. In this paper, to determine the tail state generation in various solar cell materials, we have developed a quite general theoretical scheme in which the experimental Urbach energy is compared with the absorption edge energy derived from density-functional theory (DFT) calculation. For this purpose, the absorption spectra of solar cell materials, including CdTe, $CuInSe_2$ (CISe), $CuGaSe_2$ (CGSe), $Cu_2ZnSnSe_4$ (CZTSe), Cu_2ZnSnS_4 (CZTS), and hybrid perovskites, have been calculated by DFT particularly using very-high-density k meshes. As a result, we find that the tail state formation is negligible in CdTe, CISe, CGSe, and hybrid perovskite polycrystals. However, coevaporated CZTSe and CZTS layers exhibit very large Urbach energies, which are far larger than the theoretical counterparts. Based on DFT analysis results, we conclude that the quite large tail state formation observed in the CZTSe and CZTS originates from extensive cation disordering. In particular, even a slight cation substitution is found to generate unusual band fluctuation in CZTS(Se). In contrast, $CH_3NH_3PbI_3$ hybrid perovskite shows the sharpest absorption edge theoretically, which agrees with experiment.

DOI: 10.1103/PhysRevMaterials.2.085404

I. INTRODUCTION

Potential fluctuation in the band-edge region of solar cell absorbers is quite detrimental for the performance of photovoltaic devices, reducing their open-circuit voltages (V_{oc}) rather significantly [1–4]. In particular, the creation of the tail states generally leads to serious increase of V_{oc} loss defined by $V_{loss} = E_g/e - V_{oc}$, where E_g shows the band gap of the absorber material. In fact, for hydrogenated amorphous silicon (a-Si:H), a quite large V_{loss} of ~0.8 V is observed due to the extensive tail state generation induced by the random network [5]. In contrast, high-efficiency GaAs and $Cu(In,Ga)Se_2$ solar cells exhibit small V_{loss} in a range of $0.3 \sim 0.37$ V [6,7], in part due to the lower tail state formation.

The generation of the tail state can be characterized quantitatively through the evaluation of the absorption tail generally expressed by $\alpha \propto \exp(E/E_0)$, where α is the absorption coefficient and E_0 shows the slope of the absorption tail. Specifically, E_0 obtained experimentally defines the Urbach energy ($E_0 = E_U$) [8]. It has already been reported that E_U shows a direct correlation with V_{loss} and the smaller E_U (i.e., sharper absorption edge) is favorable to suppress V_{loss} [2]. Nevertheless, since E_U is determined as a slope of experimental absorption spectra, E_U includes the contributions of the density of states (DOS) derived from (i) valence and conduction bands and (ii) nonideal tail states of absorber materials. Unfortunately, the separation of these contributions has been rather difficult and detailed E_U analyses of solar cell materials have not been performed yet.

For the detailed interpretation of material optical properties, on the other hand, density-functional theory (DFT) calculation has been performed widely [9–15]. However, such DFT analyses have so far been employed to determine E_g [9,10] and overall optical transitions in materials [9,11–15] and only a very few DFT studies have focused on the characterization of band tailing in experimental materials [16]. This is primarily because of the requirement of the complex analysis process and the extensive DFT calculation cost. Moreover, to deduce the band-edge absorption accurately in DFT, the computer calculation using high-density k points is generally necessary.

In this study, in an attempt to characterize the tail state formation and the resulting V_{oc} loss in photovoltaic devices, we have developed a general theoretical approach based on very-high-density k-mesh DFT calculations performed for various absorber materials, including binary zincblende (CdTe), ternary chalcopyrite [$CuInSe_2$ (CISe) and $CuGaSe_2$ (CGSe)], and quaternary kesterite [$Cu_2ZnSnSe_4$ (CZTSe) and Cu_2ZnSnS_4 (CZTS)] and hybrid perovskite [$CH_3NH_3PbI_3$ ($MAPbI_3$) and $HC(NH_2)_2PbI_3$ ($FAPbI_3$)] materials. By applying DFT for the absorption-spectrum calculation, DFT-derived tail absorption energy ($E_0 = E_{DFT}$) has been determined. In particular, we have evaluated the E_U/E_{DFT} ratio, from which the potential fluctuation of experimental materials is determined systematically. For CdTe, CISe, CGSe, and hybrid perovskites, the experimental absorption edges are reproduced quite well by DFT (i.e., $E_U \sim E_{DFT}$) and $MAPbI_3$ shows the sharpest band edge theoretically. In contrast, experimental

*fujiwara@gifu-u.ac.jp

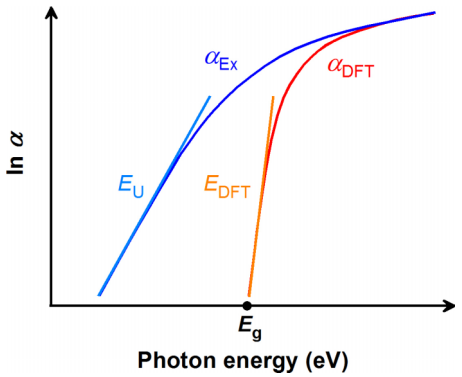

FIG. 1. Schematic representation of absorption-coefficient (α) spectra: experimental α (α_{Ex}) and DFT α (α_{DFT}) spectra. The E_U and E_{DFT} indicate the Urbach energy and DFT-derived absorption edge energy, respectively.

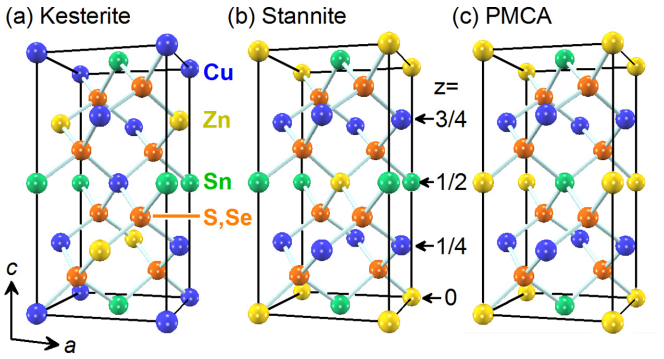

FIG. 2. Three different crystal structures of CZTS(Se) employed in the tail state analyses: (a) kesterite, (b) stannite, and (c) primitive-mixed CuAu (PMCA) structures. The arrows indicate the a and c axes of the crystals and z indicates the position of the cationic plane.

CZTSe and CZTS crystals exhibit very large tail absorption ($E_U \gg E_{DFT}$), which cannot be explained by single-phase formation of kesterite. Based on DFT analysis results, we have attributed the extraordinary large potential fluctuations observed in the CZTSe and CZTS to the tail state formation near the conduction band by cation disordering.

II. DFT ANALYSIS

A. Analysis of tail states by DFT

Figure 1 schematically shows the tail state analysis using DFT. As known well [8], the variation of α near the band-edge region can be described by

$$\alpha(E) = \alpha_0 \exp(E/E_0). \tag{1}$$

The α_{Ex} and α_{DFT} in Fig. 1 represent α obtained from experiment and DFT calculation, respectively. In general, α_{Ex} shows finite values at $E < E_g$ due to the tail state formation, and the tail energy obtained in this region defines E_U [i.e., $E_0 = E_U$ when $\alpha(E) = \alpha_{Ex}(E)$].

On the other hand, α_{DFT} becomes completely zero at $E < E_g$ and the DFT-derived absorption-edge energy can be characterized as $E_0 = E_{DFT}$ assuming $\alpha(E) = \alpha_{DFT}(E)$. It should be emphasized that E_{DFT} represents the absorption edge that originates completely from DOS of conduction and valence bands and does not include the contribution of defect states. Thus, when the tail state formation is negligible, we observe $E_U \sim E_{DFT}$, while the extensive tail state generation in experimental crystals leads to $E_U > E_{DFT}$. As a result, the evaluation of the E_U/E_{DFT} ratio enables us to separate the contribution of the conduction/valence-band states from that of the defect-derived tail states, allowing the characterization of the tail state formation theoretically.

B. DFT calculation

The DFT calculations were performed using the Vienna *Ab initio* Simulation Package (VASP) [17] as well as ADVANCE/PHASE package. For the calculations of the local density approximation (LDA) and generalized gradient approximation within the Perdew-Burke-Ernzerhof scheme (PBE), the ADVANCE/PHASE software was employed, while the VASP software was applied for hybrid functional calculations [PBE0 and Heyd-Scuseria-Ernzerhof (HSE03 and HSE06)] and PBE calculation incorporating spin-orbit coupling (SOC) interaction.

In PBE calculations without SOC, a plane-wave cutoff energy of 350 eV was used, and the structural optimization was made for all absorber crystals until the atomic configuration converged to within 5 meV/Å, except for $FAPbI_3$ (10 meV/Å). The hybrid functional calculations were carried out using a similar condition. For the DFT calculation of CdTe, a two-atom primitive cell was used, while eight-atom primitive cells were employed for the calculations of CISe, CGSe, CZTSe, and CZTS. The DFT analyses of $MAPbI_3$ [14] and $FAPbI_3$ [15] have been described in our earlier studies.

The ε_2 spectra are calculated according to

$$\varepsilon_2 = \frac{\hbar e^2}{8\pi^2 \varepsilon_0 m\omega} \int f\delta(E_{c,\mathbf{k}} - E_{v,\mathbf{k}} - \hbar\omega) d\mathbf{k}, \tag{2}$$

where E_c and E_v show the conduction- and valence-band energies. In the above equation, f represents the oscillator strength defined by

$$f = \frac{2m\omega}{\hbar} |\langle \Psi_c | \mathbf{u} \cdot \mathbf{r} | \Psi_v \rangle|^2, \tag{3}$$

where m and ω are electron mass and angular frequency of incident light, respectively. In Eq. (3), $|\Psi_c\rangle$ and $|\Psi_v\rangle$ are the conduction and valence states, where $\mathbf{u}$ and $\mathbf{r}$ represent the polarization vector and position operator, respectively. From the calculated ε_2 spectrum, the ε_1 spectrum is obtained using the Kramers-Kronig relations [8]. By employing these ε_1 and ε_2 spectra, the DFT spectra for refractive index n_{DFT} and extinction coefficient k_{DFT} are further calculated, from which α_{DFT} is finally obtained as $\alpha_{DFT} = 4\pi k_{DFT}/\lambda$.

In the DFT analyses of CZTS(Se), three different crystal structures shown in Fig. 2 were assumed: i.e., (a) kesterite, (b) stannite, and (c) primitive-mixed CuAu (PMCA) structures [18,19]. As confirmed from Fig. 2, CZTS (CZTSe) kesterite crystals are composed of the alternating atomic planes of (Cu,Sn) and (Cu,Zn) with the S (Se) atomic plane in between. The crystal structures of the stannite and PMCA phases are slightly different, and the atomic planes of the cations are separated into the Cu and (Zn,Sn) planes. In the case of PMCA, the (Zn,Sn) planes have the same ordering along the c axis.

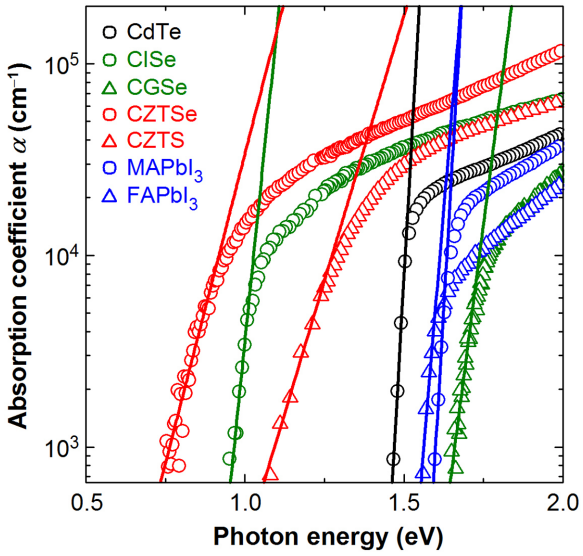

FIG. 3. Experimental α spectra of various solar cell absorbers (open circles) and the result of the Urbach analyses performed assuming $\ln\alpha \propto E/E_U$ (solid lines). For the experimental results, those reported for CdTe [20], CISe [21], CGSe [21], CZTSe [13], CZTS [22], $MAPbI_3$ [14], and $FAPbI_3$ [15] are shown.

III. RESULTS

A. Analysis of Urbach energies

Figure 3 shows experimental α spectra of various solar cell absorbers (open circles) and the result of the Urbach analyses using Eq. (1) (solid lines). For the experimental results, those reported for CdTe [20], CISe [21], CGSe [21], CZTSe [13], CZTS [22], $MAPbI_3$ [14], and $FAPbI_3$ [15] are shown. The optical data of all the materials have been obtained from the thin layers fabricated by coevaporation, except for the CdTe. The E_U of each semiconductor was estimated using a fixed α range of $600 - 4000\,\mathrm{cm}^{-1}$. The maximum range of $4000\,\mathrm{cm}^{-1}$ was chosen so that the analyzed region is below E_g, whereas the minimum range ($600\,\mathrm{cm}^{-1}$) corresponds to the sensitivity limit of ellipsometry technique used for the material characterizations [23].

All the absorbers in Fig. 3 show similar α values of $10^4\,\mathrm{cm}^{-1}$ near the E_g region. However, the CZTSe and CZTS exhibit strong tail absorption with the broad Urbach slopes, while the other materials show much sharper absorption edges, indicating the distinct tail state formation in the Cu-Zn-Sn-containing quaternary compounds. The quite broad tail absorption in CZT(S)Se has also been confirmed in earlier studies [1,24,25].

B. DFT calculation of absorption spectra

In estimating accurate α spectra by DFT, it is essential to employ a very high-density k-point mesh as described below. When high-density k-mesh calculation is performed using hybrid functionals, however, an extensive computing resource is necessary due to the quite high calculation cost of these methods. To constrain the calculation time within the manageable time scale, we calculated α_{DFT} by applying PBE. Nevertheless, the DFT calculation within PBE underestimates E_g severely [10] and thus the underestimated E_g needs to be corrected by blueshifting PBE spectrum. To confirm the validity of this approach, the band structures and optical spectra were calculated using HSE06 and PBE.

Figure 4(a) shows the band structures of CdTe calculated by HSE06 and PBE. In this figure, all the positions of the PBE conduction bands were shifted upward by ΔE_g so that E_g becomes consistent with that obtained from HSE06. When the value of $\Delta E_g = 0.7\,\mathrm{eV}$ is assumed, the shifted PBE conduction bands show excellent agreement with the conduction bands of HSE06.

In Fig. 4(b), the dielectric functions (ε_2 spectra) of CdTe calculated by HSE06 and PBE are compared with the experimental spectrum of Ref. [20]. In these calculations, an $8 \times 8 \times 8\,k$ mesh (HSE06) and $30 \times 30 \times 30\,k$ mesh (PBE) were used and the ε_2 spectra obtained from the calculations are shifted so that the onsets of the ε_2 spectra (i.e., E_0 transition) match with that of the experimental spectrum. It can be seen that the HSE06 and PBE spectra reproduce the overall experimental spectrum quite well. In particular, in the energy region between the E_0 (E_g) and E_1 transitions ($1.5 \leqslant E \leqslant 3.3\,\mathrm{eV}$), both DFT spectra are almost identical. In these DFT calculations, the small transition peak at $E = 3.9\,\mathrm{eV}$, observed experimentally, is not present, but this peak can be reproduced by incorporating the SOC interaction (see Supplemental Material Fig. 1 [26]). The result of Fig. 4(b) indicates that the optical spectrum in the band-edge transition region can be reproduced well by a shifted PBE spectrum.

To find the effect of the k-point mesh density on α_{DFT}, we further calculated f using Eq. (3). Figure 4(c) shows normalized f in the zincblende Brillouin zone of CdTe obtained using PBE. In particular, f of Fig. 4(c) was calculated for the transition from the first valence band to the first conduction band, which characterizes the band-edge absorption (see Supplemental Material Fig. 2 [27]). The numerical values for the contours (black lines) indicate the energy separation between the first valence and conduction bands, and its energy separation is consistent with the optical spectrum of Fig. 4(b). The E_0 (1.5 eV), E_1 (3.3 eV), and E_2 (5.1 eV) transitions in Fig. 4(b) correspond to the transitions at the Γ, L, and X points, respectively [28]. As confirmed from Fig. 4(c), the light absorption near E_g is highly localized near the Γ point, indicating that very-high-density k-point mesh is necessary for the accurate estimation of α_{DFT} and E_{DFT}.

In fact, when α_{DFT} was calculated by PBE using different k-point meshes [open circles in Fig. 4(d)], the absorption edge of α_{DFT} becomes sharper with increasing k-mesh density, and the E_{DFT} analysis (solid lines) also shows the reduction of E_{DFT}. In Fig. 4(e), the variations of E_{DFT} with the number of total k points in the PBE calculation are summarized. For the calculation of the two-atom primitive cell (CdTe), E_{DFT} shows a saturation trend at $k > 10^4$, whereas for eight-atom primitive cells (CISe and CZTS) and hybrid perovskites we observe the convergence at a slightly lower k of 4×10^3.

Unfortunately, the necessity of high k-point mesh density for the precise determination of E_{DFT} is very disadvantageous for HSE06 due to the quite high computational cost. In this study, therefore, we estimated α_{DFT} and E_{DFT} from shifted PBE spectra. In actual PBE calculations, we employed a $30 \times 30 \times 30\,k$ mesh for CdTe and a $16 \times 16 \times 16\,k$ mesh for the other solar cell materials, which are the maximum densities allowed in our calculation software.

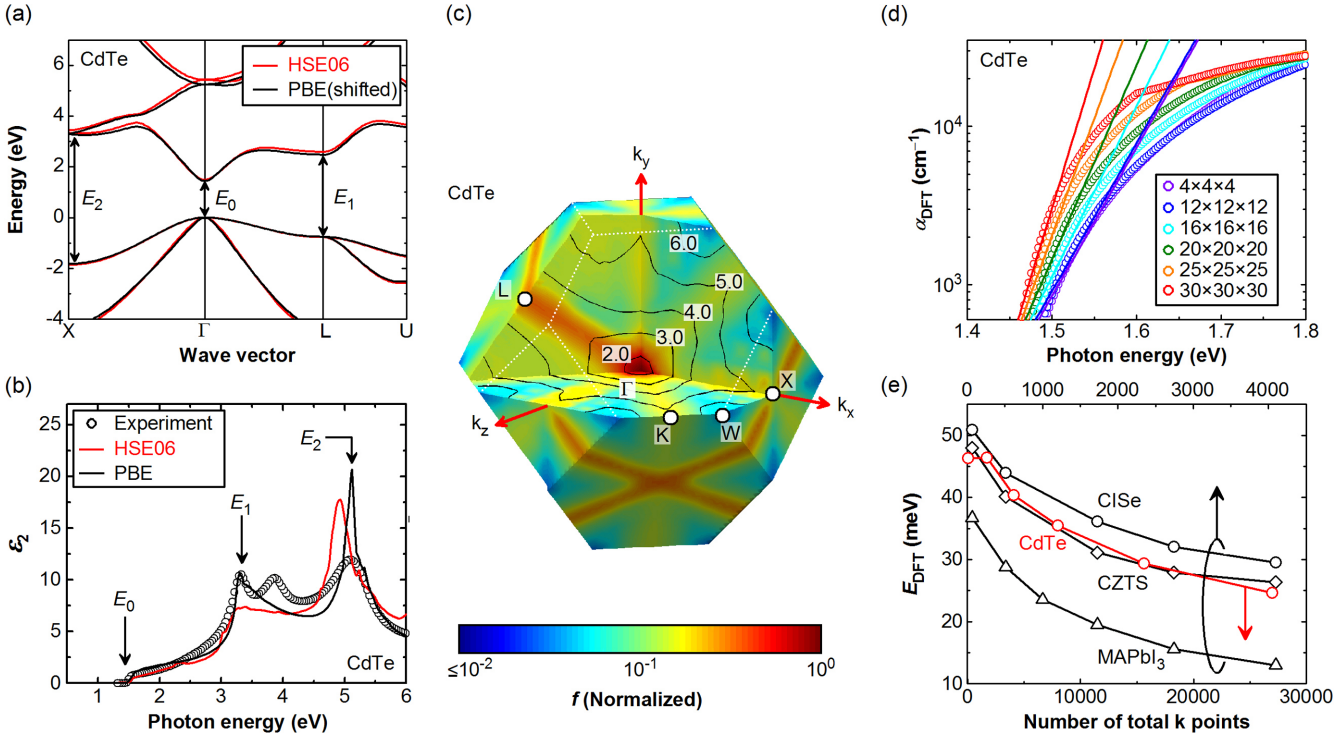

FIG. 4. (a) Band structures of CdTe calculated by HSE06 and PBE, (b) ε_2 spectra of CdTe calculated by HSE06 and PBE, (c) normalized oscillator strength (f) of CdTe in the zincblende Brillouin zone, (d) variation of α_{DFT} with k-point mesh used in the DFT calculation, and (e) variation of E_{DFT} with the number of total k points used in the DFT calculation. In (a), all the conduction bands of the PBE result are shifted upward by $\Delta E_g = 0.7$ eV. In (c), the result corresponds to f for the optical transition from the first valence band to the first conduction band. The black lines indicate the cross section of the contour for the energy separation between the first valence and conduction bands. In (d), the solid lines indicate the result of E_{DFT} analysis.

To validate our approach based on high-mesh-density PBE calculations, systematic DFT calculations were further performed for CdTe using different functionals (i.e., LDA, PBE0, HSE03, and HSE06). We find that the band structures and band-edge DOS are essentially independent of the functional, although the energy position changes depending on the functional (Supplemental Material Figs. 3(a), 3(b) [29]). Moreover, E_{DFT} shows a constant value when the screening parameter of the hybrid functional [9] is changed in a range of $\omega = 0 - 0.5\,\text{Å}^{-1}$ even though E_g varies notably (Supplemental Material Fig. 3(c) [29]). In the calculation of HSE06, for the increase of the mixing parameter a [9], α_{DFT} shifts toward higher energy but the E_{DFT} value is quite independent of a (see Supplemental Material Fig. 3(d) [29]). As a result, we have confirmed that the band-edge properties and E_{DFT} are not influenced by the type of DFT functional and the parameter values of the hybrid functional when the same k-mesh density is applied for the calculation.

C. Analysis of band tailing

Figure 5 summarizes the experimental and DFT α spectra of (a) CdTe, (b) CISe, (c) CZTSe, and (d) $MAPbI_3$, together with (e) enlarged α spectra near the E_g regions. In this figure, the energy shift values of the PBE spectra (i.e., ΔE_g) are also indicated. As shown in Fig. 5, when a high-density k mesh is employed, α_{DFT} shows excellent agreement with α_{Ex} and the overall absorption features are reproduced quite well. When the pure kesterite phase is assumed for the CZTSe, however, the agreement near the band-edge transition region is quite poor and the experimental crystal shows exceptionally large tail absorption, as indicated by the blue color region in Fig. 5(e).

For $MAPbI_3$, on the other hand, the PBE spectra calculated with and without SOC are indicated. As reported earlier [30,31], the SOC interaction alters the $MAPbI_3$ band structure significantly. In particular, when SOC is considered, the band-edge position shifts toward lower energy (Supplemental Material Figs. 4(a) and 4(b) [32]). When this E_g shift is corrected, however, the α spectrum is quite similar to that obtained without incorporating SOC.

It should be noted that, in the SOC calculation of Fig. 5(d), a smaller k-mesh density ($8 \times 8 \times 8$ k) was used due to the higher computational cost of the SOC calculation, while the calculation without SOC was implemented with a $16 \times 16 \times 16$ k, as mentioned above. Thus, the band-edge absorption is slightly broader when the SOC interaction is considered. We find, however, that the E_{DFT} values deduced with and without SOC are essentially the same when the results obtained using the same k-mesh density are compared (Supplemental Material Fig. 4(c) [32]). Accordingly, the influence of the SOC interaction on E_{DFT} is confirmed to be quite minor.

We further analyzed E_{DFT} from α_{DFT} using the α range employed to estimate E_U (i.e., $\alpha = 600 - 4000\,\text{cm}^{-1}$). Figure 6 compares E_{DFT} obtained from this procedure with E_U estimated in the analyses of Fig. 3 and all the numerical values of Fig. 6 are summarized in Table I. In Fig. 6, a

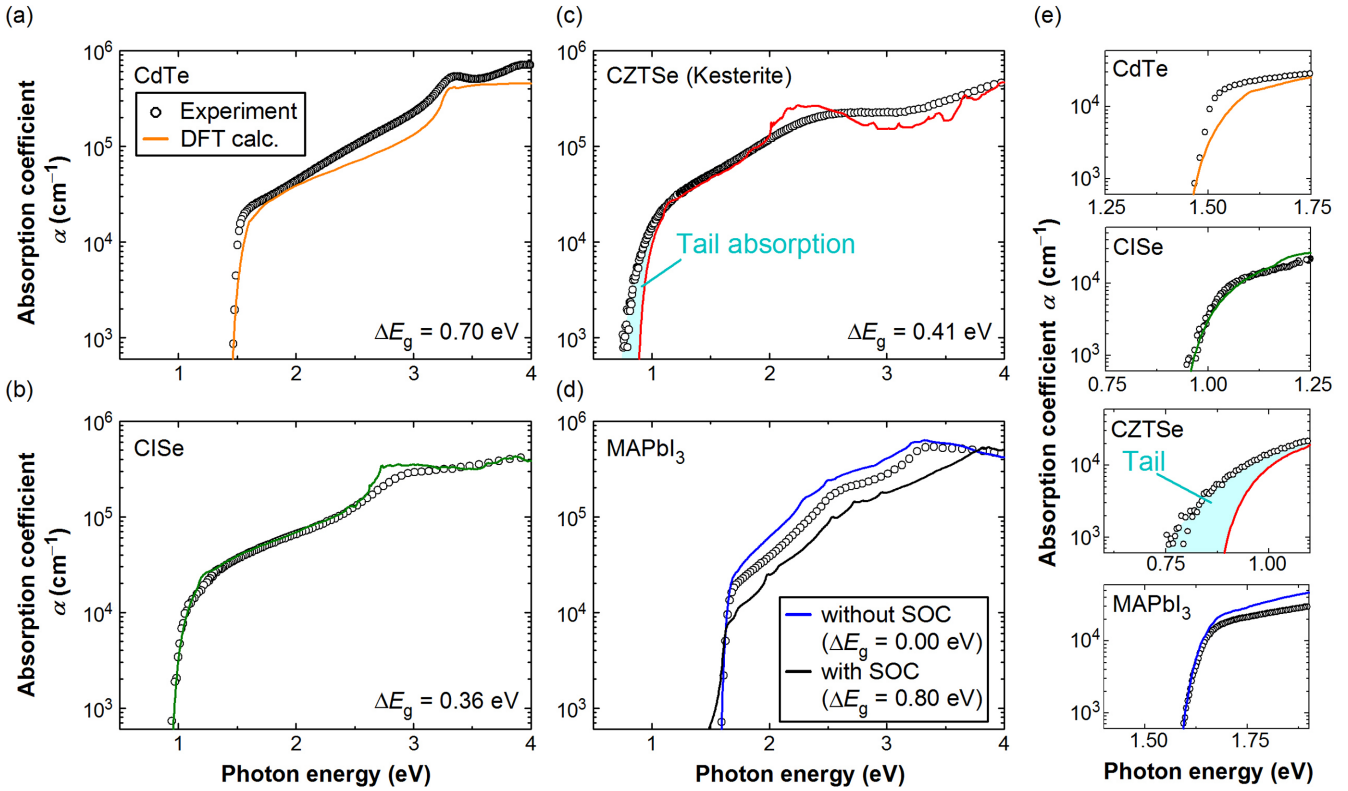

FIG. 5. α_{Ex} (open circles) and α_{DFT} (solid lines) of (a) CdTe, (b) CISe, (c) CZTSe, and (d) $MAPbI_3$, together with (e) enlarged α spectra near the E_g regions. The α_{DFT} has been shifted toward higher energy by the energy indicated as ΔE_g to improve matching with the experimental results. For the DFT calculation of CZTSe, the kesterite structure was assumed. For $MAPbI_3$, the PBE spectrum obtained by incorporating the SOC interaction is also shown.

good relationship between E_U and E_{DFT} is confirmed for the zincblende (CdTe), chalcopyrite (CISe, CGSe), and hybrid perovskite polycrystals, indicating the formation of ideal band edges in these materials. In particular, the result of $E_U \sim E_{DFT}$ is quite surprising as the DFT results are obtained assuming perfect crystal structures with zero phonon interaction (i.e., 0 K).

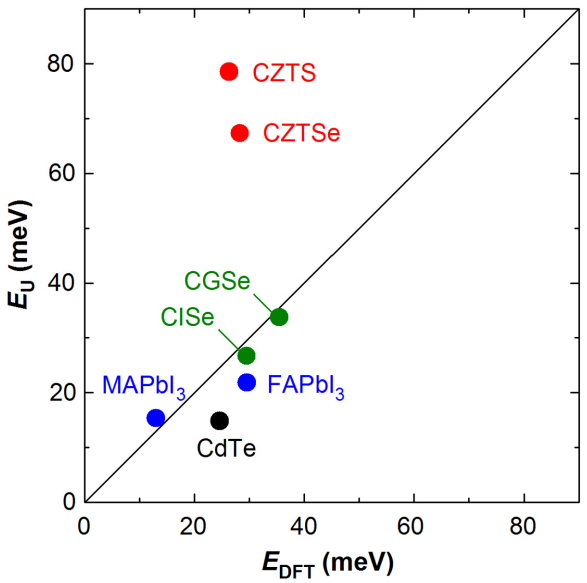

FIG. 6. Urbach energy (E_U) as a function of the absorption edge energy derived from DFT (E_{DFT}). The E_U values were estimated from the analyses of Fig. 3, whereas E_{DFT} was calculated from α_{DFT} of Fig. 5. For CZTSe and CZTS, the kesterite phases are assumed.

Among all the absorbers investigated here, $MAPbI_3$ hybrid perovskite shows the sharpest absorption edge theoretically. The quite small E_{DFT} of the hybrid perovskite, compared with the other materials, can be interpreted by the very sharp DOS distribution near the valence and conduction band edges (see Fig. 7). Moreover, E_{DFT} of $MAPbI_3$ is consistent with the experimental value of 15 meV, confirming quite suppressed tail state formation in the experimental perovskite crystal [2]. In general, E_U is quite sensitive to the potential fluctuation

TABLE I. E_U and E_{DFT} values of solar cell materials.

Materials	E_U (meV)	E_{DFT} (meV)
CdTe	14.9	24.6
CISe	26.7	29.5
CGSe	33.8	35.4
CZTS	78.5	26.4 (kesterite)
		27.3 (stannite)
		32.6 (PMCA)
CZTSe	67.3	28.3 (kesterite)
		33.4 (stannite)
$MAPbI_3$	15.4	13.0
$FAPbI_3$	21.8	29.6

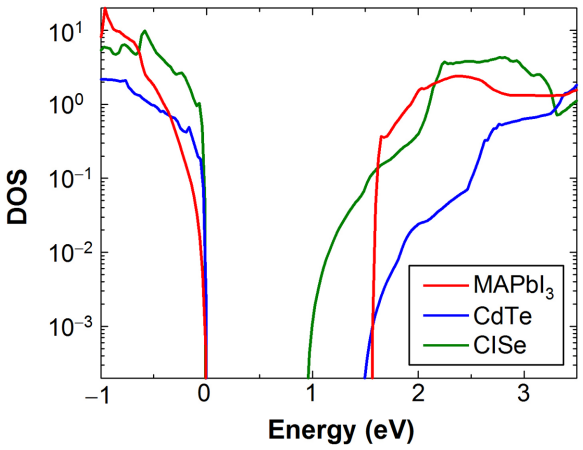

FIG. 7. DOS distribution of the valence and conduction states in $MAPbI_3$, CdTe, and CISe.

generated by (i) local band-gap variation, (ii) defects formed near the valence and conduction band edges, or (iii) displacement of atoms at polycrystalline grain boundaries. The quite small E_U of 15 meV, which agrees with the theoretical calculation, indicates clearly that none of the above tail-broadening factors are significant in experimental $MAPbI_3$ polycrystals.

In Fig. 6, on the other hand, the results for the CZTSe and CZTS are obtained assuming the pure kesterite phases. As confirmed from the results, the E_U values of the CZTSe and CZTS are far larger than E_{DFT}, indicating the exceptionally large tail state formation in these crystals. It should be emphasized that E_{DFT} of the kesterite crystal is quite similar to those of stannite and PMCA crystals (see Table I). Accordingly, the quite large E_U values observed experimentally cannot be explained by the formation of a single-phase material.

It should be emphasized that E_U of $70 - 80$ meV observed in CZTSe and CZTS is exceptionally large, as even a-Si:H having a complete random structure shows smaller E_U of $\sim$50 meV [5]. In this study, the exceptionally large E_U of the CZTSe and CZTS is attributed to the cation substitution in the experimental crystals. In particular, we performed first quantitative analysis for the tail absorption observed experimentally in CZTS(Se) based on the DFT calculations.

To validate our hypothesis that the quite extensive tail state formation in the CZTSe and CZTS is induced by the cation disordering, the α_{DFT} spectra of the stannite and PMCA phases are obtained and the α spectrum for a kesterite-stannite-PMCA mixed phase is calculated as a simple weighted average of the three α_{DFT} spectra obtained from the kesterite, stannite, and PMCA crystals by neglecting the interaction among the three phases. As shown in Figs. 2(a) and 2(b), the configurations of the Sn and S(Se) atoms in the kesterite and stannite crystals are identical and the Cu-Zn ordering distinguishes these phases. On the other hand, the crystal structure of PMCA is quite close to that of the stannite, as mentioned earlier.

Figure 8(a) shows α_{Ex} (open circles) and the simulated α spectrum (red line) of CZTS. In this figure, the α_{DFT} spectra of the kesterite, stannite, and PMCA phases, obtained using the same energy shift value of $\Delta E_g = 0.40$ eV, are also shown. As reported previously [18,19,33], the stannite and PMCA crystals have slightly smaller E_g, compared with the kesterite crystal,

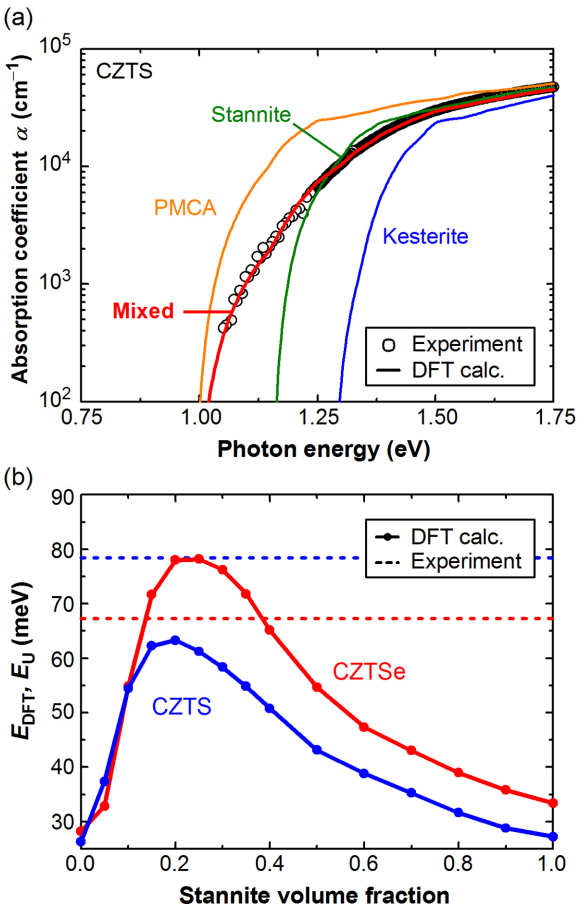

FIG. 8. (a) α_{DFT} spectra of CZTS obtained assuming the kesterite, stannite, PMCA, and three-phase-mixed structures (solid lines), together with α_{Ex} (open circles) and (b) variation of E_{DFT} with stannite volume fraction in CZTSe and CZTS. In (a), the experimental data are consistent with Fig. 3. In (b), the E_U positions are indicated by the dotted lines.

and the whole α spectra of the stannite and PMCA are redshifted by 0.13 and 0.31 eV in Fig. 8(a), respectively. Accordingly, the formation of a mixed-phase crystal leads to the large tail absorption by the overlap of the three α spectra. The red line in Fig. 8(a) represents the simulation result obtained from the fitting analysis assuming the three-phase mixture and, when we assume the volume ratio of kesterite:stannite:PMCA $= 0.35 \pm 0.10 : 0.45 \pm 0.05 : 0.20 \pm 0.05$, the calculated result shows excellent agreement with the experimental result.

Importantly, there has been no clear evidence that the large tail state absorption in CZTS is caused by cation mixing. As confirmed from Fig. 8(a), our DFT-based analysis provides a semiempirical result that the extensive cation substitution in CZTS generates the quite strong tail absorption in a wide energy range near E_g. More complete descriptions for the cation disordering in CZTS can be found in Sec. IV B.

Figure 8(b) shows the variation of E_{DFT} with stannite volume fraction in CZTSe and CZTS. For this calculation, the kesterite-stannite two-phase composite is assumed. In the figure, the experimental E_U values are also indicated by the dotted lines. Rather surprisingly, E_{DFT} shows a rapid increase up to the stannite fraction of 20 vol.% at which E_{DFT} of the CZTSe

becomes comparable to E_U. In the case of CZTS, experimental E_U cannot be reproduced by the two-phase mixture and thus the three-phase crystal structure was assumed. The result of Fig. 8(b) indicates that the slight cation disordering induces a quite large increase of E_U in CZT(S)Se and the quite strong tail absorption can quantitatively be explained by the band-gap fluctuation generated by the extensive cation mixing.

IV. DISCUSSION

A. Defect formation in CZTS and CZTSe

So far, a variety of point and complex defects have been proposed to be generated within CZTS(Se) crystals [34–41]. Among those, a defect created by Cu-Zn cation exchange (i.e., $Cu_{Zn} + Zn_{Cu}$) shows the lowest formation energy for the majority of the chemical potential range [36]. In fact, there has been a strong consensus that $Cu_{Zn} + Zn_{Cu}$ is the most likely defect in CZTS(Se) and the $Cu_{Zn} + Zn_{Cu}$ formation is more energetically favorable, compared with point defects of Cu_{Zn} and Zn_{Cu} [36,41]. It should be emphasized that the tail absorption observed in CZTS(Se) is quite strong with the α values of $10^3 \sim 10^4\,cm^{-1}$ (see Fig. 3) and the low-concentration defects are very unlikely to induce the strong tail absorption confirmed in CZTS(Se).

At some chemical potential conditions, however, Cu_{Zn} antisite defects (i.e., Zn site replaced with Cu) form more easily [36]. Nevertheless, the formation energy of Cu_{Zn} increases drastically under the Cu-poor and Zn-rich conditions [36], which have typically been employed for the fabrication of high-efficiency CZTS and CZTSe solar cells [35,36]. For a CZTS layer fabricated under the Cu-poor and Zn-rich condition, a quite high E_U of 85 meV, comparable to those of the CZTSe and CZTS layers having near-stoichiometric compositions (Fig. 6), has been confirmed [25]. Accordingly, the compositional modulation does not appear to alter E_U and it is unlikely that Cu_{Zn} defects induce the strong tail absorption in CZTS(Se).

On the other hand, the presence of a Cu-vacancy defect complex ($V_{Cu} + Zn_{Cu}$) has been confirmed experimentally [38]. However, the DFT calculations show that the formation of this defect complex leads to a slight increase of the effective band gap [36,37,39] and the generation of the tail state absorption by these defects is not plausible. In addition, the V_{Cu} states are created very close to the valence band ($\leqslant$20 meV from the valence band) [34,36] and we also ruled out the possibility that the extensive tail absorption is generated by V_{Cu} defects.

In CZTS(Se), the formation of $2Cu_{Zn} + Sn_{Zn}$ defect complex has also been proposed [35]. Nevertheless, this is a deep-level defect and the population range of the defect is predicted to be $10^{11} \sim 10^{18}\,cm^{-3}$ [36], which is apparently too small to induce the strong tail absorption. Systematic DFT studies have shown that the formation energies of other defects are quite high [36] and the densities of these defects are expected to be low. Based on the above considerations, the exceptionally large absorption observed below E_g of CZTS and CZTSe has been attributed to $Cu_{Zn} + Zn_{Cu}$ defects in this study.

B. Cation disorder in CZTS and CZTSe

Quite early DFT studies implemented on CZTS and CZTSe confirmed that the kesterite is the most probable crystal structure for CZTS(Se) [18,33]. Nevertheless, the total energies of the kesterite, stannite, and PMCA phases are quite similar and the formation of the stannite and PMCA phases by cation intermixing was expected to occur [18,33]. Later, however, such pictures are denied almost completely by detailed structural characterization of experimental CZTS(Se) crystals based on neutron diffraction [42], resonant x-ray diffraction [43], scanning transmission electron microscopy [44], and nuclear magnetic resonance [45] experiments, and only kesterite-based crystals are found to be formed, although slight cation mixing does occur in the Cu-Zn atomic planes of the kesterite [i.e., the cationic plane position of $z = 1/4$ and $3/4$ along the c axis in Fig. 2(a)] [42–45].

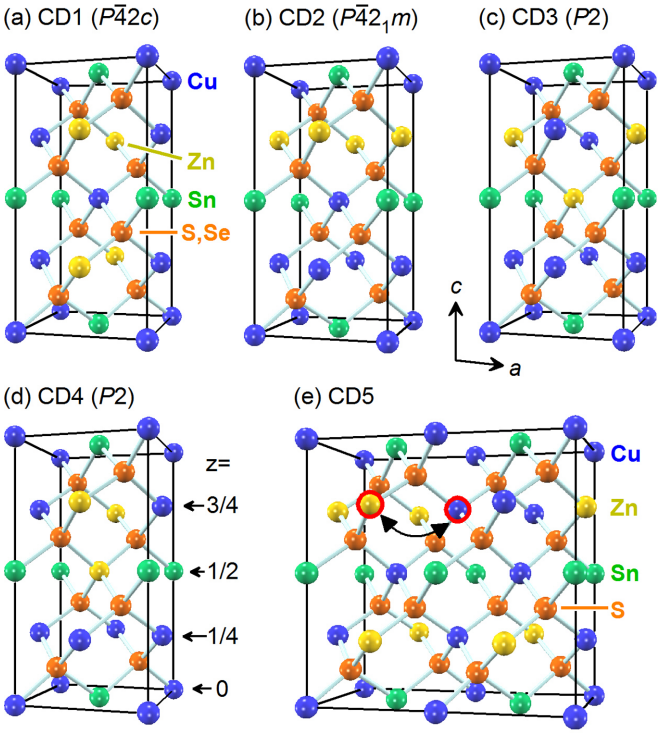

FIG. 9. Cation-disordered structures of CZTS for a 16-atom cell. In a 32-atom supercell shown in (e), one pair of Cu and Zn atoms indicated by the red circles is replaced assuming a kesterite structure.

However, we emphasize that all the results that conclude the kesterite phase formation without the inclusion of the stannite and PMCA phases have been obtained from the single crystals formed at high temperatures (~800 °C) with sufficient time. In coevaporated CZTS(Se) layers formed at lower temperatures, the cation disordering can be very different from those observed in the single crystals. In order to further support our conclusion that the extraordinary tail absorption observed in coevaporated CZTS and CZTSe layers originates from quite extensive cation substitutions, we have performed DFT calculations for various cation-disordered phases shown in Fig. 9.

With the crystals of Fig. 2, the crystal structures shown in Figs. 9(a)–9(d) complete the different cation-disordered (CD) structures in a 16-atom cell. The crystal structure of Fig. 9(a) can be considered as the kesterite phase with a disordered Cu-Zn plane at a $z = 3/4$ position. In the cation-disordered

TABLE II. Lattice parameters (a, b, c), crystal distortion ($\eta = c/2a$), E_g, and total energy difference (ΔE_t) of different CZTS crystal structures shown in Figs. 2 and 9.

Structure	a (Å)	b (Å)	c (Å)	$\eta(c/2a)$	E_g (eV)[a]	ΔE_t (meV/atom)
Kesterite	5.552	5.552	10.982	0.989	1.281	0.0
Stannite	5.548	5.548	11.010	0.992	1.153	3.6
PMCA	5.530	5.530	11.054	0.999	0.972	4.5
CD1	5.553	5.553	10.998	0.990	1.266	0.5
CD2	5.557	5.557	11.091	0.998	1.063	24.3
CD3	5.556	5.554	11.010	0.991	0.921	16.9
CD4	5.555	5.556	11.013	0.991	0.915	16.9
CD5	11.104	5.554	10.989	0.990[b]	1.217	4.5

[a]Calculated by PBE assuming a E_g correction of 0.40 eV.
[b]Calculated from c/a.

structures of Figs. 9(b)–9(d), Cu and Zn planes (CD2) and unique Zn clustered structures (CD3, CD4) are created. We also assumed a cation-disordered structure that is obtained by exchanging one Cu atom with one Zn atom in a 32-atom kesterite supercell structure [CD5 of Fig. 9(e)], as suggested from the structural studies of the single crystals.

Table II summarizes the lattice parameter, crystal distortion ($\eta = c/2a$), E_g, and total energy difference (ΔE_t) of all the CZTS crystals shown in Figs. 2 and 9. All the CZTS results were deduced based on the PBE calculation using an $8 \times 8 \times 4$ k mesh for a 16-atom-cell and a $4 \times 8 \times 4$ mesh for a 32-atom cell. In the table, the underestimated E_g values in the PBE calculations were corrected by adding 0.40 eV as estimated in the analysis of Fig. 8(a), whereas ΔE_t values were obtained as a difference from the kesterite structure (i.e., $\Delta E_t = 0$ in the kesterite). Figure 10 further shows α_{DFT} of all the CZTS crystals.

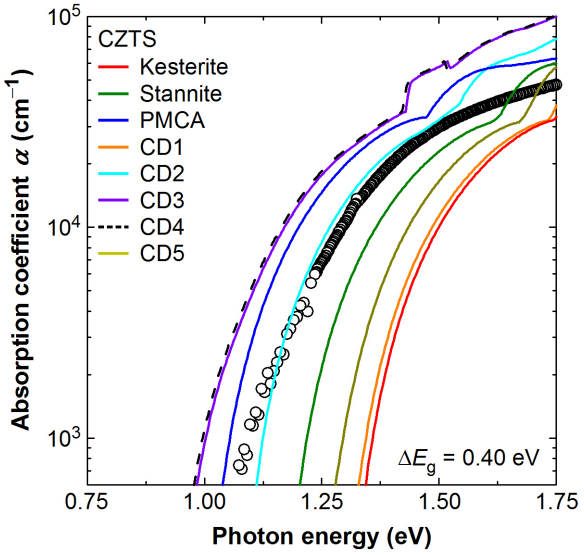

FIG. 10. α spectra calculated for different CZTS crystal structures shown in Figs. 2 and 9 (solid lines) and α spectrum obtained from experiment (open circles).

As mentioned above, in the single crystals, the cation mixing occurs only in the limited planes (i.e., at $z = 1/4$ and $3/4$). Specifically, in the case of the 16-atom cell, only the kesterite and CD1 structures are allowed and ΔE_t of CD1 is almost identical to that of the kesterite. However, CD1 indicates E_g and α_{DFT} very similar to those of the kesterite and thus the incorporation of the CD1 phase into the kesterite host crystal does not generate the large tail absorption confirmed in the experiment. When the Zn-plane and Zn-clustered structures are formed (i.e., CD2–CD4 in Table II), on the other hand, E_g shifts significantly to lower energies with the redshift of the whole α spectra. Nevertheless, these crystals show remarkable increase in ΔE_t and therefore it is quite unlikely that these phases are formed in experimental crystals. In particular, when the Zn atomic plane is created (CD2), ΔE_t shows a very high value.

When one pair of the Cu and Zn atoms is replaced in the 32-atom structure (CD5), E_g shifts only slightly by 64 meV toward lower energy, compared with the kesterite. In this structure, ΔE_t also increases due to the local clustering of Cu and Zn atoms. It should be emphasized that, when the cation mixing at $z = 1/4$ and $3/4$ is assumed in a 32-atom supercell, only the pure kesterite [i.e., Fig. 2(a)], CD1 and CD5 structures are allowed. In these structures, there is only a weak E_g shift and thus the cation substitution within the limited cationic planes cannot explain the large tail absorption observed for CZTS(Se).

In earlier studies, the link between the strong tail absorption and cation disordering in CZTS(Se) has been overlooked and our result indicates that the large tail state absorption confirmed experimentally in coevaporated CZTS(Se) layers can best be explained by the mixed-phase formation of the kesterite/stannite/PMCA crystal structures that show the small ΔE_t values among the possible cation-disordered phases. Although the tail state absorption could still be generated by the incorporation of other cation-mixed phases, ΔE_t values of such phases tend to be high [46] and the generation of such phase becomes energetically more difficult.

C. Potential fluctuation in CZTS

To find the effect of the tail state formation on the solar cell performance more clearly, we calculated the band alignment of the different CZTS crystal structures shown in Figs. 2 and 9. In our calculations, the core-level corrections were made simply using the $4d$ level of the Sn atom [47]. Figure 11 summarizes the band alignments of the CZTS crystals. In this result, the conduction-band positions have been shifted upward by $\Delta E_g = 0.40$ eV to compensate the underestimated E_g in the PBE calculations.

It can be seen from Fig. 11 that the incorporation of the stannite and PMCA phases into the kesterite leads to the formation of the localized states just below the conduction-band minimum as reported for Cu_2ZnGeS_4 [19]. A similar result has also been confirmed for the kesterite and stannite crystals of CZTSe. Based on the above result, we conclude that the extraordinary large E_U observed in the CZTS and CZTSe originates primarily from the extensive tail states formed near the conduction-band edge.

On the other hand, the conduction- and valence-band positions of the CD1 structure are almost identical to those of the kesterite structure. Furthermore, in the cation-disordered

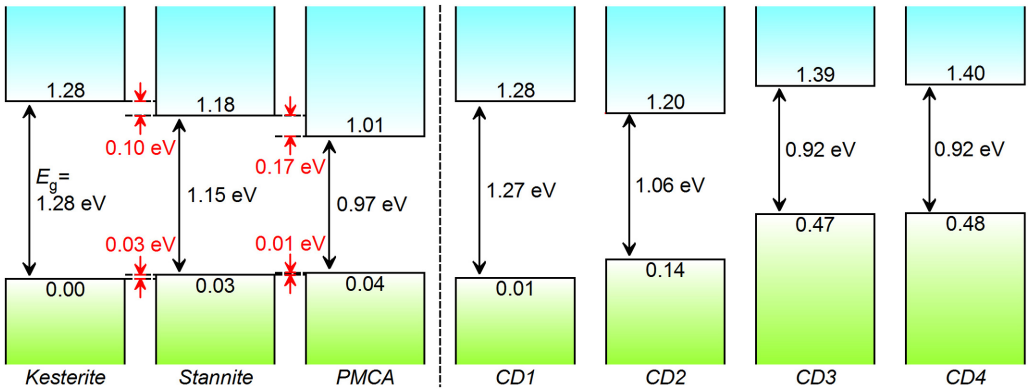

FIG. 11. Band alignments for different CZTS crystal structures shown in Figs. 2 and 9. In the figure, the conduction-band positions have been shifted upward by $\Delta E_g = 0.40$ eV to compensate the underestimated E_g in the PBE calculations. The numerical values shown within each band represent the relative energy positions of each band.

phases of CD2−CD4, the E_g reduction occurs by the upward shift of the valence-band positions and this trend is quite different from that of the stannite and PMCA structures. Due to high ΔE_t of the CD2−CD4 structures, however, we ruled out the formation of these phases.

In CZTS, a conduction-band offset created in a kesterite/stannite/PMCA mixture is quite large with $\Delta E_c = 0.27$ eV (see Fig. 11). In other words, the tail absorption in a CZTS crystal extends in a wide energy region of ∼0.3 eV below E_g, as confirmed directly from the experimental result of Fig. 3. Unfortunately, conventional CZTS(Se) solar cells are fabricated using p-type CZTS(Se) absorbers and thus the minority carriers in the solar cells are electrons. In this case, the tail states formed near the conduction band are expected to act as trap sites for electrons and are quite detrimental in the operation of the solar cells.

D. V_{oc} deficit in CZTS solar cells

In CZTS, a quite large V_{loss} of ∼0.8 eV has been reported [41,48]. In conventional solar cells including GaAs and Cu(In,Ga)Se_2, V_{loss} is in a range of 0.3 ∼ 0.4 V (see Sec. I) and V_{loss} of CZTS is higher by 0.4 ∼ 0.5 V. We attributed this additional V_{oc} deficit observed in CZTS solar cells primarily to the band-gap fluctuation within the conduction band (ΔE_c ∼ 0.3 eV) due to extensive cation disordering.

Unfortunately, the interpretation of the significant V_{loss} in CZTS(Se) has been controversial and the following has been suggested as the causes of V_{loss} (or performance loss): (i) the electrostatic potential fluctuation induced by charge states [1,37,41,49–52], (ii) the Cu-Zn cation substitution [46], (iii) the formation of deep defects ($2Cu_{Zn} + Sn_{Zn}$) [35,40], and (iv) the defect formation at the CdS/CZTS(Se) front interface [53,54]. So far, many earlier studies proposed the presence of a strong electrostatic potential fluctuation, characterized by the parallel shift of a constant band gap due to spatial variation of charged defects [1,37,41,49–52]. Such conclusions have been drawn mainly from the detailed analysis of photoluminescence (PL) spectra [49–52]. Nevertheless, PL characterizes the light emission, rather than the light absorption, and the anomalous tail absorption in CZTS(Se) has not been considered in these studies.

The band-gap fluctuation by cation mixing was also suggested previously [46]. However, in a recent experimental study that modulated the cation disorder in CZTSSe devices by changing the cooling rate after lower-temperature annealing, the effect of the cation disorder on V_{oc} (or band-gap fluctuation) has been concluded to be very small (∼40 mV) and the cation mixing as a cause of the large V_{loss} has been denied [41]. In the study, however, the influence of the quite strong band tailing has been neglected almost completely.

At this stage, only limited analyses have been performed to clarify the effect of the defect formation on V_{loss} [54] and more quantitative studies are necessary to determine its contribution on V_{oc}. As evidenced in this study, however, the energy range of the extensive tail formation (∼0.3 eV below the fundamental band gap) can explain very large V_{loss} confirmed in CZTS devices. Accordingly, the suppression of the strong cation disordering is expected to be crucial for the further improvement of CZTS(Se) solar cells.

V. SUMMARY

The absorption edge energies of various solar cell absorber materials, including CdTe, CISe, CGSe, CZTS, CZTSe, and hybrid perovskite compounds, have been calculated by DFT to determine the tail state formation in the absorber materials. Very-high-density k meshes have been used in these DFT calculations to characterize the absorption edge accurately. The absorption-edge energy deduced from the DFT calculations indicates an excellent correlation with the Urbach energy, confirming the formation of ideal sharp band edges in experimental crystals. In particular, $MAPbI_3$ hybrid perovskite shows the sharpest absorption edge theoretically, indicating superior band-edge transition properties of this material. In contrast, we observe that the Urbach energies of polycrystalline CZTSe and CZTS are far larger than the theoretical values. The very large Urbach energies observed experimentally in CZTS(Se) have been attributed to the cation substitution, which in turn generates the tail state formation near the conduction-band edge. In particular, for the CZTS, by taking a weighting average of three DFT α spectra obtained for kesterite, stannite,

and PMCA phases, the experimental α spectrum has been reproduced. As a result, our theoretical approach is found to be quite effective in determining band tailing originating from imperfect crystal formation.

[1] T. Gokmen, O. Gunawan, T. K. Todorov, and D. B. Mitzi, Appl. Phys. Lett. **103**, 103506 (2013).

[2] S. D. Wolf, J. Holovsky, S.-J. Moon, P. Löper, B. Niesen, M. Ledinsky, F.-J. Haug, J.-H. Yum, and C. Ballif, J. Phys. Chem. Lett. **5**, 1035 (2014).

[3] C. J. Hages, N. J. Carter, and R. Agrawal, J. Appl. Phys. **119**, 014505 (2016).

[4] U. Rau, B. Blank, T. C. M. Müller, and T. Kirchartz, Phys. Rev. Appl. **7**, 044016 (2017).

[5] R. A. Street, *Hydrogenated Amorphous Silicon* (Cambridge University Press, Cambridge, England, 1991).

[6] M. A. Green, K. Emery, Y. Hishikawa, W. Warta, E. D. Dunlop, D. H. Levi, and A. W. Y. Ho-Baillie, Prog. Photovolt. **25**, 3 (2017).

[7] T. Kato, Jpn. J. Appl. Phys. **56**, 04CA02 (2017).

[8] J. I. Pankove, *Optical Processes in Semiconductors* (Dover, New York, 1971).

[9] F. Bechstedt, *Many-Body Approach to Electronic Excitations: Concepts and Applications* (Springer, Heidelberg, 2015).

[10] M. Marsman, J. Paier, A. Stroppa, and G. Kresse, J. Phys.: Condens. Matter **20**, 064201 (2008).

[11] F. Kootstra, P. L. de Boeij, and J. G. Snijders, Phys. Rev. B **62**, 7071 (2000).

[12] J. Paier, M. Marsman, and G. Kresse, Phys. Rev. B **78**, 121201 (2008).

[13] Y. Hirate, H. Tampo, S. Minoura, H. Kadowaki, A. Nakane, K. M. Kim, H. Shibata, S. Niki, and H. Fujiwara, J. Appl. Phys. **117**, 015702 (2015).

[14] M. Shirayama, H. Kadowaki, T. Miyadera, T. Sugita, M. Tamakoshi, M. Kato, T. Fujiseki, D. Murata, S. Hara, T. N. Murakami, S. Fujimoto, M. Chikamatsu, and H. Fujiwara, Phys. Rev. Appl. **5**, 014012 (2016).

[15] M. Kato, T. Fujiseki, T. Miyadera, T. Sugita, S. Fujimoto, M. Tamakoshi, M. Chikamatsu, and H. Fujiwara, J. Appl. Phys. **121**, 115501 (2017).

[16] B. Sadigh, P. Erhart, D. Åberg, A. Trave, E. Schwegler, and J. Bude, Phys. Rev. Lett. **106**, 027401 (2011).

[17] G. Kresse and J. Furthmüller, Phys. Rev. B **54**, 11169 (1996).

[18] S. Chen, X. G. Gong, A. Walsh, and S.-H. Wei, Appl. Phys. Lett. **94**, 041903 (2009).

[19] S. Chen, X. G. Gong, A. Walsh, and S.-H. Wei, Phys. Rev. B **79**, 165211 (2009).

[20] *Spectroscopic Ellipsometry for Photovoltaics, Volume 2: Applications and Optical Data of Solar Cell Materials*, edited by H. Fujiwara and R. W. Collins (Springer, Heidelberg, 2018).

[21] S. Minoura, K. Kodera, T. Maekawa, K. Miyazaki, S. Niki, and H. Fujiwara, J. Appl. Phys. **113**, 063505 (2013).

[22] J. Li, H. Du, J. Yarbrough, A. Norman, K. Jones, G. Teeter, F. L. Terry, and D. Levi, Opt. Express **20**, A327 (2012).

[23] H. Fujiwara, *Spectroscopic Ellipsometry: Principles and Applications* (Wiley, West Sussex, 2007).

[24] M. M. Islam, M. A. Halim, T. Sakurai, N. Sakai, T. Kato, H. Sugimoto, H. Tampo, H. Shibata, S. Niki, and K. Akimoto, Appl. Phys. Lett. **106**, 243905 (2015).

[25] M. Valentini, C. Malerba, F. Menchini, D. Tedeschi, A. Polimeni, M. Capizzi, and A. Mittiga, Appl. Phys. Lett. **108**, 211909 (2016).

[26] See Supplemental Material at http://link.aps.org/supplemental/10.1103/PhysRevMaterials.2.085404 for ε_2 spectrum calculated by PBE with SOC interaction.

[27] See Supplemental Material at http://link.aps.org/supplemental/10.1103/PhysRevMaterials.2.085404 for the optical transition analysis of CdTe.

[28] S. Adachi, *Optical Constants of Crystalline and Amorphous Semiconductors: Numerical Data and Graphical Information* (Kluwer Academic Publishers, Norwell, 1999).

[29] See Supplemental Material at http://link.aps.org/supplemental/10.1103/PhysRevMaterials.2.085404 for the variation of the calculation result with the DFT functional.

[30] J. Even, L. Pedesseau, J.-M. Jancu, and C. Katan, J. Phys. Chem. Lett. **4**, 2999 (2013).

[31] P. Umari, E. Mosconi, and F. D. Angelis, Sci. Rep. **4**, 4467 (2014).

[32] See Supplemental Material at http://link.aps.org/supplemental/10.1103/PhysRevMaterials.2.085404 for the calculation result of $MAPbI_3$ with SOC interaction.

[33] J. Paier, R. Asahi, A. Nagoya, and G. Kresse, Phys. Rev. B **79**, 115126 (2009).

[34] A. Walsh, S. Chen, S.-H. Wei, and X.-G. Gong, Adv. Energy Mater. **2**, 400 (2012).

[35] S. Chen, L.-W. Wang, A. Walsh, X. G. Gong, and S.-H. Wei, Appl. Phys. Lett. **101**, 223901 (2012).

[36] S. Chen, A. Walsh, X.-G. Gong, and S.-H. Wei, Adv. Mater. **25**, 1522 (2013).

[37] A. Polizzotti, I. L. Repins, R. Noufi, S.-H. Wei, and D. B. Mitzi, Energy Environ. Sci. **6**, 3171 (2013).

[38] M. Paris, L. Choubrac, A. Lafond, C. Guillot-Deudon, and S. Jobic, Inorg. Chem. **53**, 8646 (2014).

[39] D. Huang and C. Persson, Thin Solid Films **535**, 265 (2013).

[40] M. Grossberg, T. Raadik, J. Raudoja, and J. Krustok, Curr. Appl. Phys. **14**, 447 (2014).

[41] S. Bourdais, C. Choné, B. Delatouche, A. Jacob, G. Larramona, C. Moisan, A. Lafond, F. Donatini, G. Rey, S. Siebentritt, A. Walsh, and G. Dennler, Adv. Energy Mater. **6**, 1502276 (2016).

[42] S. Schorr, Sol. Energy Mater. Sol. Cells **95**, 1482 (2011).

[43] A. Lafond, L. Choubrac, C. Guillot-Deudon, P. Fertey, M. Evain, and S. Jobic, Acta Crystallogr. B **70**, 390 (2014).

[44] B. G. Mendis, M. D. Shannon, M. C. J. Goodman, J. D Major, R. Claridge, D. P. Halliday, and K. Durose, Prog. Photovolt. **22**, 24 (2014).

[45] L. Choubrac, M. Paris, A. Lafond, C. Guillot-Deudon, X. Rocquefelte, and S. Jobic, Phys. Chem. Chem. Phys. **15**, 10722 (2013).

[46] J. J. S. Scragg, J. K. Larsen, M. Kumar, C. Persson, J. Sendler, S. Siebentritt, and C. P. Björkman, Phys. Status Solidi B **253**, 247 (2016).

[47] C. Persson and A. Zunger, Phys. Rev. B **68**, 073205 (2003).

[48] A. Nakane, H. Tampo, M. Tamakoshi, S. Fujimoto, K. M. Kim, S. Kim, H. Shibata, S. Niki, and H. Fujiwara, J. Appl. Phys. **120**, 064505 (2016).

[49] M. J. Romero, H. Du, G. Teeter, Y. Yan, and M. M. Al-Jassim, Phys. Rev. B **84**, 165324 (2011).

[50] C. J. Hages, N. J. Carter, R. Agrawal, and T. Unold, J. Appl. Phys. **115**, 234504 (2014).

[51] K. F. Tai, T. Gershon, O. Gunawan, and C. H. A. Huan, J. Appl. Phys. **117**, 235701 (2015).

[52] J. Márquez-Prieto, M. V. Yakushev, I. Forbes, J. Krustok, P. R. Edwards, V. D. Zhivulko, O. M. Borodavchenko, A. V. Mudryi, M. Dimitrievska, V. Izquerdo-Roca, N. M. Pearsall, and R. W. Martin, Sol. Energy Mater. Sol. Cells **152**, 42 (2016).

[53] I. L. Repins, J. V. Li, A. Kanevce, C. L. Perkins, K. X. Steirer, J. Pankow, G. Teeter, D. Kuciauskas, C. Beall, C. Dehart, J. Carapella, B. Bob, J.-S. Park, and S.-H. Wei, Thin Solid Films **582**, 184 (2015).

[54] A. Crovetto, M. Palsgaard, T. Gunst, T. Markussen, K. Stokbro, M. Brandbyge, and O. Hansen, Appl. Phys. Lett. **110**, 083903 (2017).